Geometric Acoustics for Aircraft Noise Scattering

Yueping Guo[1] and Russell H. Thomas[1]
NASA Langley Research Center, Hampton, VA 23681, USA

This paper discusses aircraft noise scattering by geometric acoustics, which consists of the basic features of sound propagation and reflection in rays or ray tubes, diffraction by smooth geometry in terms of surface creeping waves, and diffraction by abrupt geometry features such as the wing trailing edges. Based on the classic theories of these features, prediction methodologies can be constructed for aircraft noise scattering. The methodologies, however, require important modifications and extensions to account for unique features in aircraft noise applications, for both current conventional aircraft and future unconventional designs. These modifications and extensions include the derivation of a general reflection coefficient that contains the effects of surface geometry curvature, surface impedance, and mean flow. Corrections to the basic formulation of diffraction, for both smooth geometry and sharp edges, are formulated to account for the finite dimensions of practical applications. For smooth geometry diffraction, a second-order correction is used to continuously transition from insonified to shadow zones and an approach is presented to compute the properties of the geodesic path of surface wave propagation. A model is developed to make use of the ray propagation formulation for incoherent and partially coherent propagation and scattering, which is an important phenomenon in aircraft noise. Mean flow effect is also included in the methodology for low Mach number flows. Examples of calculations based on these theoretical developments are presented to illustrate the unique features in aircraft noise applications.

Nomenclature

A	=	sound wave amplitude
A_D	=	diffraction integral
a	=	radius of curvature
B_{ij}	=	geometry coefficients in reflection coefficient
C_R	=	reflection coefficient
c_0	=	mean sound speed
D	=	diffraction coefficient
E	=	acoustic energy
$\mathbf{e}_i$	=	local coordinate system unit vector
F	=	gradually varying integrand function
G	=	Green's function
k_0	=	acoustic wavenumber
M_i	=	Mach number component in surface coordinates
M_r	=	Mach number component in microphone direction
$\mathbf{M}$	=	Mach number vector
$\mathbf{n}$	=	unit surface normal vector
p	=	acoustic pressure
p_D	=	diffracted acoustic pressure
p_I	=	incident acoustic pressure
p_R	=	reflected acoustic pressure
q	=	source strength
Q	=	source autocorrelation
R	=	surface to microphone distance modified by flow
R_s	=	surface to source distance modified by flow

[1] Senior Research Engineer, Aeroacoustics Branch, AIAA Associate Fellow.

r = microphone distance
$\hat{\mathbf{r}}$ = microphone direction unit vector
r_m = surface to microphone distance
r_s = surface to source distance
$\hat{\mathbf{r}}_s$ = source direction unit vector
s = arc length or wedge line length coordinate
s^* = wedge line length at diffraction point
$\mathbf{s}$ = wedge line unit vector
s_0 = arc length of geodesic path
S = scattering surface
s_i = surface curvilinear coordinates
$\mathbf{t}_i$ = surface tangent vector
w = wedge angle
$\mathbf{x}$ = field coordinates
$\mathbf{x}_b$ = beginning point of geodesic path or wedge line
$\mathbf{x}_c$ = cross section shape coordinates
$\mathbf{x}_e$ = ending point of geodesic path or wedge line
$\mathbf{x}_g$ = geodesic path coordinates
$\mathbf{x}_s$ = source coordinates
$\mathbf{x}_v$ = virtual microphone coordinates on coincidence line
$\mathbf{x}_w$ = wedge line coordinates
$\mathbf{y}$ = surface coordinates
$\mathbf{y}^*$ = stationary point coordinates
Z = acoustic impedance
β = Mach number factor
β_R = Mach number factor involving reflection direction
η = surface wave loss factor
θ_I = incidence angle
κ = surface curvature
Λ = determinant of the second derivative tensor
μ = decay factor in second order correction
ν = wedge index
ρ = microphone to wedge line distance
ρ_0 = mean density
ρ_s = source to wedge line distance
σ = signature of the second derivative tensor
τ = time delay
φ = microphone azimuthal angle
φ_s = source azimuthal angle
Φ = acoustic wave phase function
ϕ = acoustic velocity potential
Ψ = phase function of integrand function
Π = acoustic pressure spectrum

I. Introduction

Geometric acoustics has been researched extensively in the past and has been applied in various areas in acoustics [1]-[9]. The basic principles of the theory and its limitations and favorable features are well documented and discussed. The main limitation is its high frequency asymptotic formulation, limiting its applications to cases where the acoustic wavelength is smaller than the characteristic length scale of the scattering geometry. Despite this limitation, geometric acoustics remains an attractive method in practical applications because of its favorable features, which include its intuitive formulation of rays and ray tubes that closely mimic the physical propagation of sound waves, its ability to accommodate complex surface geometries, and its high computation efficiency. The last is still a critical requirement for practical aircraft noise applications even with the drastic improvements of computing power of modern computers in recent years; it is orders of magnitude more efficient than any other numerical methods, such as the volume discretization method of Computational Aeroacoustics (CAA) and the surface discretization method of Boundary

Element Method (BEM), and it is the only method feasible for quick turn-around engineering applications of full configuration aircraft for the most important frequencies in the kilohertz range. Because of this, geometric acoustics has attracted attention in recent years for aircraft noise applications [10]-[14]. The use of geometric acoustics in aircraft noise scattering, however, is not a simple matter of straightforward application. The basic theories need to be modified and/or extended to account for the unique features.

Motivated by the favorable features of the method of geometric acoustics, this paper presents a methodology within its framework, with emphasis on aircraft noise applications. The methodology contains the three basic elements, ray tracing for propagation and reflection, surface creeping wave diffraction for smooth geometry, and sharp wedge diffraction for abrupt geometry features. Since the basic concepts of these elements are well-established, the focus of the paper will be the new developments, the modifications, and the extensions that are tailored for aircraft noise applications.

Aircraft applications involve complex geometry of curved surfaces. In addition, the surfaces are sometimes treated with acoustic liners for noise reduction and the geometry is embedded in nonuniform flows. These features are essential and can affect the reflection of acoustic waves, and thus, affect the noise scattered by the aircraft. A general formulation of the reflection coefficient will be presented, derived by asymptotic analysis, and including all these effects, in closed form analytical formulas to allow for efficient numerical implementation. It will be shown that in the general case of curved surfaces with impedance conditions and the presence of mean flow, the incident and the reflected sound follow Fermat's principle that the incidence angle and the reflection angle are equal. The reflection coefficient, however, is determined jointly by the surface properties and the flow. The derived reflection coefficient will be validated in two ways. The first is applying the general form to some simpler cases for which the reflection coefficient can be found by other independent methods. It will be shown that the results for the simpler cases are exactly recovered by the general formulation. The second way of validation is applying the derived results to cases where numerical solutions are available for comparison. Examples will be presented to show the accuracy of the asymptotic formula. Comparisons will also be given with the panel reflection approximation, which may seem to be logical since geometric acoustics often discretizes the surfaces of the geometry into panels but results in large errors.

The smooth geometry and the sharp wedge diffraction use the classical theories [16]-[23], with the surface creeping wave generation and radiation for smooth geometry and the wedge diffraction for abrupt geometry. The concepts are physically intuitive, and the theories are well developed for canonical geometries. In adapting the theories for aircraft noise, use can be made of the fact that the scattering geometry contains elongated elements, such as the wing leading and trailing edges and the fuselage, characterized by approximately invariant cross sections over a range of many wavelengths in the length direction. Thus, the smooth geometry diffraction can be formulated by long cylindrical surfaces of irregular cross sections, for which the classic diffraction theory can be applied. To this end, a method will be presented to efficiently derive or compute the properties of the helical waves on the diffraction surfaces, including the path of the surface wave propagation, the phase changes of the waves along the propagation path, and the amplitude decay of the surface waves, which control the diffracted sound.

For sharp geometry diffraction, the analytical solutions for semi-infinite wedges will be adapted as the starting point for trailing edge diffraction. The basic theory for the canonical geometry is in analytical form and will be cast in a format consistent with ray tracing. However, corrections are needed to account for the effects of finite dimensions of the aircraft geometry. This will be done by approximate models, derived from simple considerations of the scattering configurations. The approximate models are acceptable for engineering applications because the finite dimension effects are of second order under the framework of geometric acoustics, where the dimensions of the scattering surfaces are larger than the acoustic wavelength. Comparisons between the asymptotic results, the analytical solutions, and the Kirchhoff approximation [14]-[17] will be given for the simple canonical problem of sound diffraction by a semi-infinite plate, demonstrating the accuracy of the asymptotic results and the shortfall of the Kirchhoff method.

Many aircraft noise sources are only partially coherent. This poses a challenge for numerical methods such as CAA and BEM, because the computation of such methods gives the total acoustic pressure at the measurement locations without information on how the sound propagates from its sources to the measurement locations, and thus, the results always imply perfectly coherent sources when the pressures are squared to construct the noise spectra. Since geometric acoustics follows individual rays, or propagation paths, source coherence can be naturally accounted for because the differences in ray path lengths represent different source times of the ray contributions. The source coherence effects can then be calculated by the differences in ray path lengths when the ray contributions are summed at the measurement locations. The formulation of the coherence effects under the framework of geometric acoustics is analytical, but empirical models will be introduced to characterize the constructive and destructive interferences of various ray contributions. Examples will be given to illustrate the importance of source coherence modeling, together with comparisons with wind tunnel test data.

II. Reflection

The reflection of sound by a surface involves the determination of the reflection location on the surface, the reflection direction, and the reflection coefficient. For the simple case of a rigid flat plate, the reflection is governed by the Fermat's principle that the incidence angle and the reflection angle are equal, and the reflection coefficient is simply unity. For general configurations of irregularly shaped geometry with nonzero surface curvature in the presence of mean flows and with surface treatments, exact solutions in closed analytical form are not feasible. Asymptotic solutions can be derived by starting with the formulation of the reflection problem by the Green's theorem. The process starts with the frequency domain convective wave equation for the acoustic pressure

$$\nabla^2 p - \left(-\mathrm{i}k_0 + \mathbf{M}\cdot\nabla\right)^2 p = q \tag{1}$$

where the acoustic pressure is denoted by p, the frequency is represented by the acoustic wavenumber, $k_0=\omega/c_0$, with ω and c_0 being the angular frequency and the mean sound speed, respectively, the mean flow is given by the Mach number vector, **M**, and the source distribution is defined by q. Solutions to this equation are subject to the boundary conditions on the scattering body surfaces. It is convenient and useful to allow acoustic treatment on local areas of the surfaces, typically described as the surface impedance condition and written as

$$\frac{\rho_0 c_0}{\mathrm{i}k_0 Z}\left(-\mathrm{i}k_0 + \mathbf{M}\cdot\nabla\right)^2 p + \mathbf{n}\cdot\nabla p = 0 \quad \text{on} \quad S \tag{2}$$

where ρ_0 is the mean density, Z is the surface impedance as a function of frequency, **n** is the unit normal vector of the body surface pointing into the acoustic medium, and S is the scattering surface. The scattering geometry is illustrated in Fig. 1 where the source is indicated by its coordinate $\mathbf{x}_s$ and the surface S is a function of the surface coordinate **y** represented by the two curvilinear coordinates, s_1 and s_2. In general, both the Mach number and the surface impedance can depend on the spatial coordinates, the former because of nonuniform flows and the latter due to locally treated surfaces. In the framework of geometric acoustics, however, variations of both are assumed to be gradual, compared to the sound wave variations within a wavelength. Furthermore, the reflection of the incident waves is a local feature about the reflection point. Thus, both these parameters can be treated as constant, and the governing equations are to be solved for results in the local region.

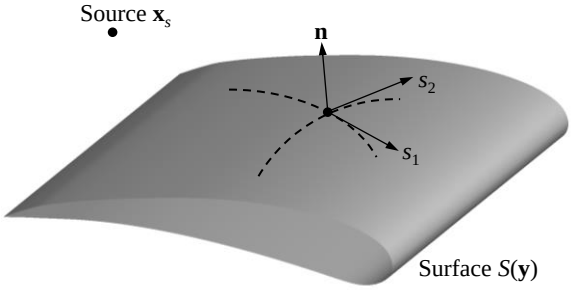

Fig. 1 Illustration of scattering surface integration.

By following the standard approach of the Green's theorem, the solution that is subject to the radiation condition in the far field can be derived in terms of an integral equation

$$p(\mathbf{x}) = p_I(\mathbf{x}) + \int_{S(\mathbf{y})} \left(p\mathbf{n}\cdot\nabla G - G\mathbf{n}\cdot\nabla p\right) dS(\mathbf{y}) \tag{3}$$

where p_I is the incident field and G is the free space Green's function given by

$$G(\mathbf{x}-\mathbf{y}) = \frac{1}{4\pi R} e^{\mathrm{i}k_0 \Phi} \tag{4}$$

where R denotes the distance between the surface point **y** and the field point **x**, modified by the mean flow, as a function of **x** - **y**, defined by

$$R(\mathbf{x}-\mathbf{y}) = \sqrt{\beta^2 \left|\mathbf{x}-\mathbf{y}\right|^2 + \left((\mathbf{x}-\mathbf{y})\cdot\mathbf{M}\right)^2} \tag{5}$$

and the phase function Φ is given by

$$\Phi(\mathbf{x}-\mathbf{y}) = \frac{1}{\beta^2}\left[R(\mathbf{x}-\mathbf{y}) - \mathbf{M}\cdot(\mathbf{x}-\mathbf{y})\right] \tag{6}$$

with β^2 denoting 1-**M**·**M**.

The result (3) can be cast into a form that is more appropriate for deriving the reflection coefficient. For this purpose, the boundary condition (2) can be used to eliminate the gradient term in the integrand function. The total acoustic pressure, present on both sides of the integral representation (3), can then be regarded locally as the sum of an incidence and a reflection component, leading to

$$p_R(\mathbf{x}) = \int_{S(\mathbf{y})} \left(\mathbf{n}\cdot\nabla G + G\frac{\rho_0 c_0}{\mathrm{i}k_0 Z}\left(-\mathrm{i}k_0 + \mathbf{M}\cdot\nabla\right)^2 \right)\left(p_I + p_R\right) dS(\mathbf{y}) \tag{7}$$

where p_R is the reflected field. By carrying out the gradients of the Green's function, the reflected pressure becomes

$$p_R(\mathbf{x}) = \int_{S(\mathbf{y})} G\left[\left(\frac{\mathrm{i}k_0}{\beta^2} - \frac{1}{R}\right)\mathbf{n}\cdot\nabla R + \frac{\rho_0 c_0}{\mathrm{i}k_0 Z}\left(-\mathrm{i}k_0 + \mathbf{M}\cdot\nabla\right)^2 \right]\left(p_I + p_R\right) dS(\mathbf{y}) \,. \tag{8}$$

This is an exact integral representation of the acoustic reflection problem formulated by the governing equation (1) and the boundary condition (2). It is not, however, an explicit solution because the unknown reflected pressure appears in the integrand function on the right-hand side. For general geometric shapes, the integral equation is unlikely to have closed form exact analytical solutions.

To apply asymptotic analysis to the result (8), the integral on the right-hand side can be symbolically cast in the form of

$$p_R(\mathbf{x}) = \int_{s_1}\int_{s_2} \frac{1}{4\pi R} F(\mathbf{y}) A(\mathbf{y}) e^{\mathrm{i}k_0\psi(\mathbf{y})} ds_1 ds_2 \tag{9}$$

where the integration over the surface S has been written out explicitly in terms of the two orthogonal curvilinear coordinates on the surface, namely, s_1 and s_2, as shown in Fig. 1. Thus, the surface coordinate $\mathbf{y}$ becomes a function of these two arc length parameters, $\mathbf{y} = \mathbf{y}(s_1, s_2)$. The amplitude function F is written for

$$F(\mathbf{y}) = \left(\frac{\mathrm{i}k_0}{\beta^2} - \frac{1}{R}\right)\mathbf{n}\cdot\nabla R + e^{-\mathrm{i}k_0\Phi(\mathbf{y}-\mathbf{x}_s)}\frac{\rho_0 c_0 R_s}{\mathrm{i}k_0 Z}\left(\mathrm{i}k_0 - \mathbf{M}\cdot\nabla\right)^2 \frac{e^{\mathrm{i}k_0\Phi(\mathbf{y}-\mathbf{x}_s)}}{R_s} \tag{10}$$

where Φ is defined by (6). The phase function of the integrand function in (9) is defined by

$$\psi = \frac{1}{\beta^2}\left[R + R_s - \mathbf{M}\cdot(\mathbf{x}-\mathbf{x}_s)\right]. \tag{11}$$

The symbol R_s has been introduced to save writing. It stands for $R_s = R(\mathbf{y}\text{-}\mathbf{x}_s)$ with the definition of R given by the definition (5). The distance between the surface point $\mathbf{y}$ and the source location $\mathbf{x}_s$ modified by the flow effects. The symbolic expression also involves rewriting the pressure terms as the amplitude term A and an exponential phase factor, namely,

$$p_I + p_R = A(\mathbf{y}) e^{\mathrm{i}k_0\Phi(\mathbf{y}-\mathbf{x}_s)} \,. \tag{12}$$

The result (9) is cast in a form where the rapid oscillations of the integrand function are controlled by the exponential factor with the remaining integrand being a smoothly varying function. In the limit of large k_0, as consistent with geometric acoustics, the rapid oscillations of the exponential factor result in mutual cancellations of the contributions from the individual surface integration elements, except at the location of $\mathbf{y}$ where the gradients of the phase function vanish, for which the cancellations are not complete. This is the essence of the method of stationary phase, which is a well-documented mathematical method [6], [24] so that only the necessary details are given here. At the stationary point, denoted by $\mathbf{y}=\mathbf{y}^*$, it follows that

$$\nabla\psi\cdot\frac{\partial\mathbf{y}}{\partial s_1} = \nabla\psi\cdot\frac{\partial\mathbf{y}}{\partial s_2} = 0 \tag{13}$$

where ∇ is the gradient operation with respect to $\mathbf{y}$. The solution at the stationary point is given by

$$p_R(\mathbf{x}) = F(\mathbf{y}^*)A(\mathbf{y}^*)\frac{1}{2k_0 R\sqrt{|\Lambda|}} e^{\mathrm{i}\left[k_0\psi(\mathbf{y}^*)+\sigma\pi/4\right]}. \tag{14}$$

Here the quantity Λ is the determinant of the second derivative tensor of the phase function, defined by

$$\Lambda = \frac{\partial^2\psi}{\partial s_1^2}\frac{\partial^2\psi}{\partial s_2^2} - \left(\frac{\partial^2\psi}{\partial s_1 \partial s_2}\right)^2 \tag{15}$$

and evaluated at the stationary phase point. The quantity σ is the signature of Λ [24].

The amplitude quantity A is defined by (12) and introduced to separate the oscillating part of the acoustic pressures from their gradually varying parts, which enables the integrand function in (9) to be cast in a form convenient for the

application of the method of stationary phase. With the asymptotic solution derived by (14), this amplitude quantity can be eliminated by substituting back the acoustic pressures, which leads to

$$p_R(\mathbf{x}) = F(\mathbf{y}^*)\Big[\, p_I(\mathbf{y}^*) + p_R(\mathbf{y}^*)\,\Big]\frac{1}{2k_0 R\sqrt{|\Lambda|}}\, e^{\mathrm{i}\left[k_0\Phi(\mathbf{x}-\mathbf{y}^*)+\sigma\pi/4\right]}. \tag{16}$$

The asymptotic method reduces the integral equation (9) to the algebra equation (16), with the unknown reflected pressure appearing on both sides of the result. This is, however, not an ordinary algebraic equation because the independent variables of the reflected pressure are different on the two sides of the equation, being the microphone location $\mathbf{x}$ on the left-hand side and the stationary phase point $\mathbf{y}^*$ on the surface on the right-hand side.

To proceed, the stationary phase point of the surface integration in (9) needs to be derived, defined by the vanishing of the derivatives of the phase function (11), with respect to the integration variables, as specified by (13). Since the surface coordinates are parameterized by the arc lengths, the derivatives of the coordinates with respect to the curvilinear arc lengths are simply the unit tangent vectors of the surface. Thus, simplified notations can be used for the derivatives of the coordinate vectors in the result (13), namely, $\mathbf{t}_i = \partial\mathbf{y}/\partial s_i$ with $\mathbf{t}$ being the unit tangential vector and i = 1 and 2, respectively, denoting the two surface curvilinear coordinates. By carrying out the two gradient operations in (13), some mathematical manipulations can reduce the results to

$$\frac{r}{R}\left(\mathbf{M}\cdot\hat{\mathbf{r}}\right) + \frac{r_s}{R_s}\left(\mathbf{M}\cdot\hat{\mathbf{r}}_s\right) = 0\,. \tag{17}$$

This equation can be solved to find

$$\left(\mathbf{M}\cdot\hat{\mathbf{r}}\right) + \left(\mathbf{M}\cdot\hat{\mathbf{r}}_s\right) = 0 \tag{18}$$

which simply states that the projection of Mach number vector in the source direction is the opposite of its projection in the microphone direction. By substituting this back into (17), it immediately follows that $r/R = r_s/R_s$. Thus, it can be shown that the stationary phase conditions are simply

$$\cos\theta_I = \hat{\mathbf{r}}\cdot\mathbf{n} = \hat{\mathbf{r}}_s\cdot\mathbf{n} \tag{19}$$

where the incidence angle is represented by θ_I. In these results, r and r_s are the distances from the stationary point $\mathbf{y}^*$ to the field point $\mathbf{x}$ and the source point $\mathbf{x}_s$, respectively. The distance vectors of the two are denoted respectively by the bold face symbols and the overhead circumflex means unit vector.

The meaning of the stationary point becomes clear from these results. At the stationary phase point, the sum of the two unit vectors, pointing in the source and the microphone directions from the stationary point, respectively, is normal to the two surface tangents, which in turn implies that the sum is parallel to the surface normal. Furthermore, since the unit vectors represent the direction from the surface point $\mathbf{y}$ to the field point $\mathbf{x}$ and to the source point $\mathbf{x}_s$, respectively, the unit vectors must make an equal angle with the surface normal. This is precisely Fermat's principle of reflection. The stationary point on the surface in the current mathematical formulation is exactly such a reflection point. The derivations have included the effects of mean flow and surface impedance with the classic Fermat's principle for a static medium precisely recovered.

The phase function for the surface integration (9) is given by the expression (11). Its second derivatives can be found by straightforward differentiation, with the result

$$\frac{\partial^2\psi}{\partial s_i\partial s_j} = \frac{r^2(r+r_s)}{r_s R^3}B_{ij} \tag{20}$$

with the coefficients B_{11} and B_{22} introduced to save writing, which are defined by

$$B_{ii} = -\frac{r_s r\beta_R^2}{r+r_s}\frac{\partial^2\mathbf{y}}{\partial s_i^2}\cdot(\hat{\mathbf{r}}+\hat{\mathbf{r}}_s) + \beta^2\sin^2\alpha_i + M_r^2 + M_i^2 - 2M_iM_r\cos\alpha_i \tag{21}$$

for i =1 and 2, and similarly, $B_{12} = B_{21}$, given by

$$B_{12} = -\frac{r_s r\beta_R^2}{r+r_s}\frac{\partial^2\mathbf{y}}{\partial s_1\partial s_2}\cdot(\hat{\mathbf{r}}+\hat{\mathbf{r}}_s) + M_1M_2 - \beta^2\cos\alpha_1\cos\alpha_2 - M_r\left(M_2\cos\alpha_1 + M_1\cos\alpha_2\right) \tag{22}$$

where angles α_1 and α_2 are the angles between the reflection direction and the two curvilinear coordinate directions, defined by $\hat{\mathbf{r}}\cdot\mathbf{t}_i = \cos\alpha_i$ (i=1,2). Since the component of the mean flow velocity normal to the surface is zero, the vector Mach number can be expressed in terms of its two components parallel to the surface, namely, $\mathbf{M} = M_1\mathbf{t}_1 + M_2\mathbf{t}_2$ and the component M_r is written for $M_r = \hat{\mathbf{r}}\cdot\mathbf{M}$. The quantity β_R is written for the square root of $\beta^2 + (\hat{\mathbf{r}}\cdot\mathbf{M})^2$. The incidence angle is denoted by θ_I and defined by (19). With these notations, the result (16) can be rewritten as

$$p_R(\mathbf{x}) = \left[\, p_I(\mathbf{y}^*) + p_R(\mathbf{y}^*) \,\right] F(\mathbf{y}^*) \frac{r_s}{r + r_s} \frac{\beta_R^2}{2k_0 \sqrt{\left| B_{11}B_{22} - B_{12}^2 \right|}} e^{\mathrm{i}\left[k_0 \Phi(\mathbf{x}-\mathbf{y}^*) + \sigma\pi/4 \right]}. \tag{23}$$

The reflected pressure appears on both sides of this result, and it is evaluated at different spatial locations with the left-hand side at the field point **x** and the right-hand side at the stationary point $\mathbf{y}^*$ on the surface. To explicitly find the reflection coefficient, the field coordinate **x** is set to formally approach the stationary phase point $\mathbf{y}^*$, namely, $r \to 0$. In this limit, the first terms in the coefficients B_{11}, B_{22} and B_{12} vanish. It can be shown that

$$B_{11}B_{22} - B_{12}^2 \to \beta_R^2 \cos^2\theta_I \tag{24}$$

which simplifies the result (23) to

$$p_R(\mathbf{y}^*) = \left[\, p_I(\mathbf{y}^*) + p_R(\mathbf{y}^*) \,\right] F(\mathbf{y}^*) \frac{\mathrm{i}\beta_R}{2k_0 \cos\theta_I}. \tag{25}$$

This equation can be solved to find the reflection pressure at the stationary phase point with the result

$$p_R(\mathbf{y}^*) = p_I(\mathbf{y}^*) \frac{\mathrm{i}\beta_R F(\mathbf{y}^*)}{2k_0 \cos\theta_I - \mathrm{i}\beta_R F(\mathbf{y}^*)}. \tag{26}$$

When this is substituted back into the solution (23) for the reflection pressure at any microphone location, it leads to the explicit solution in terms of the reflection coefficient

$$p_R(\mathbf{x}) = p_I(\mathbf{y}^*) C_R \frac{r_s}{r + r_s} e^{\mathrm{i}k_0 \Phi(\mathbf{x}-\mathbf{y}^*)} \tag{27}$$

where the reflection coefficient is denoted by C_R and is given by

$$C_R = \frac{\cos\theta_I F(\mathbf{y}^*)}{2k_0 \cos\theta_I - \mathrm{i}\beta_R F(\mathbf{y}^*)} \frac{\beta_R^2}{\sqrt{\left| B_{11}B_{22} - B_{12}^2 \right|}} e^{\mathrm{i}\sigma\pi/4}. \tag{28}$$

The quantity F in this result can be found from its definition (10) by carrying out explicitly the derivative operations. In the derivations, simplifications can be made in consistency with the high frequency asymptotical analysis, by only retaining the leading order terms in the results. This greatly reduces the algebraic expression, but is not an additional approximation in the analysis, and if needed, all terms can be retained. Thus, the reflection coefficient can be further written as

$$C_R = \frac{Z\beta^4 \beta_R \cos\theta_I - \rho_0 c_0 \left(\beta_R - M_r \right)^2}{Z\beta^4 \beta_R \cos\theta_I + \rho_0 c_0 \left(\beta_R - M_r \right)^2} \frac{\beta_R \cos\theta_I}{\sqrt{\left| B_{11}B_{22} - B_{12}^2 \right|}} e^{\mathrm{i}(\sigma-2)\pi/4}. \tag{29}$$

The reflection coefficient is now an explicit formula given by the surface geometry, the incidence and the reflection direction, the local mean flow Mach number, and the surface impedance. Furthermore, the explicit solution (27) is in the form of geometric acoustics with the reflected acoustic pressure in the field given by the incident pressure at the reflection point on the surface, the reflection coefficient, the divergence due to propagation, and the phase function. The derivations of these results are subject to the same high frequency asymptotic approximations of geometric acoustics.

III. Validation of Reflection Coefficient

The general solution for the reflection coefficient (29) can be reduced to simpler forms for specific canoniccal geometric shapes. The canonical problems may not have significant practical applications but can be valuable as validations for the asymptotic solutions because they can be derived by other independent methods. A few cases are presented in this section, some of which have analytical formulas for the reflection coefficient derived by alternative methods, while others have analytical solutions for the total and/or reflected pressure.

The simplest case is a flat plate, for which the curvatures, and hence, the second derivatives of the surface coordinates in (21) and (22), are zero. The remaining terms can then be substituted into the solution (29), reducing the reflection coefficient to

$$C_R = \frac{Z\beta^4 \beta_R \cos\theta_I - \rho_0 c_0 \left(\beta_R - M_r \right)^2}{Z\beta^4 \beta_R \cos\theta_I + \rho_0 c_0 \left(\beta_R - M_r \right)^2} \tag{30}$$

which is the reflection coefficient for flat plates with surface impedance in uniform mean flows. For a static medium, the Mach number quantity can be set to zero and the quantity B_R becomes unity, leading to the coefficient of flat plates with surface impedance but without flow,

$$C_R = \frac{Z\cos\theta_I - \rho_0 c_0}{Z\cos\theta_I + \rho_0 c_0}. \tag{31}$$

Furthermore, for a rigid plate, the impedance is infinite so that the reflection coefficient reduces further to

$$C_R = 1. \tag{32}$$

These results can be derived by wavenumber integrations in the limit of large microphone distance and/or high frequency [6], [7]. They are recovered precisely by the asymptotic solution (29), providing a validation for these canonic cases.

For a rigid cylinder of general arbitrary cross section in a static medium, simplifications to the asymptotic solution (29) can be made by setting the mean flow Mach number to zero and the second derivatives of the geometry coordinate with respect to the axial direction also to zero. Without loss of generality, the s_1 coordinate can be chosen to be the axial direction. Thus, the parameters given by (21) and (22) reduce to

$$\begin{aligned} B_{11} &= \sin^2\alpha_1 \\ B_{22} &= -\frac{r_s r}{r+r_s}\frac{\partial^2 \mathbf{y}}{\partial s_2^2}\cdot(\hat{\mathbf{r}}+\hat{\mathbf{r}}_s) + \sin^2\alpha_2 \\ B_{12} &= -\cos\alpha_1\cos\alpha_2 \end{aligned}. \tag{33}$$

The quantity B_{22} can be further simplified by writing the second derivative in terms of the surface curvature, namely,

$$\frac{\partial^2 \mathbf{y}}{\partial s_2^2}\cdot(\hat{\mathbf{r}}+\hat{\mathbf{r}}_s) = 2\cos\theta_I \frac{\partial^2 \mathbf{y}}{\partial s_2^2}\cdot\mathbf{n} = 2\kappa\cos\theta_I \tag{34}$$

where κ denotes the surface curvature. With this, it follows that

$$C_R = \sqrt{\frac{(r+r_s)\cos\theta_I}{(r+r_s)\cos\theta_I + 2\kappa r_s r\sin^2\alpha_2}}. \tag{35}$$

This result can also be derived by using the variational principle on the geometrical reflection of acoustic rays for a rigid cylindrical surface in a static medium [4], validating the asymptotic results derived here.

In addition to applying the general formula to simple cases to recover the analytical results derived by other independent methods, the asymptotic formulations can also be validated in cases where numerical solutions are available for comparison. An example of such cases is the sound scattering by a circular cylinder, for which formal solutions can be found in terms of an infinite series modal summation in the circumferential direction and a wavenumber integration in the axial direction. Both can be computed numerically. The solutions can include mean flow effects in the axial direction and surface impedance, and thus, can provide validations for various parametric trends. The systematic validations of parametric variations are not the focus here and will be reported in a future study. Instead, the analytical solutions are used here only to highlight the importance of the reflection coefficient derived in the previous section. For this purpose, the problem is set up as shown in Fig. 2 (not to scale), where a source is positioned 2 radii from the cylinder center and a group of microphones is arranged on a circular arc of radius equal to 10 radii of the cylinder. The microphones are 4 radii away from the source in the downstream direction.

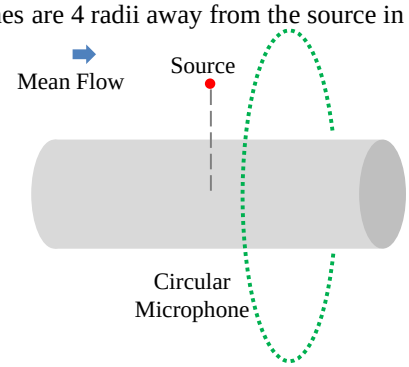

Fig. 2 Configuration of acoustic reflection by circular cylinder.

The comparisons between the asymptotic results and the analytical solutions are shown in Fig. 3, where the difference in sound pressure levels (ΔSPL), between the total sound pressure and the incident sound pressure, is plotted as a function of the azimuthal angle, which is defined to be zero in the source direction and 180 degrees on the opposite side of the cylinder from the source. The results shown in the figure are at 1000 Hz with a mean flow Mach number of 0.4. The length parameters in the calculation are normalized by the cylinder radius so that the results can be interpreted as for a cylinder radius of 1 meter. Since the configuration is symmetric with respect to the source location,

only half of the azimuthal angular domain is shown in the figure. The analytical solutions are plotted by the green solid curve, and the asymptotic results of the geometric acoustics are shown by the red dash-dot curve, which uses the curved surface reflection coefficient (29) derived in the previous sections. For comparison, results by geometric acoustics using panel reflection are also shown in the figure by the dashed blue curve. The comparison with the analytical solution shows that the formulation derived in the previous section has high accuracy in most of the angular domain. The errors between the asymptotic and the analytical solutions become noticeable at angles close to about 150 degrees. This is the transition region from the insonified to the shadow region. The coincidence angle at which the incident ray is tangential to the surface is 144.26 degrees for the configuration considered here, beyond which there is no reflection. At this condition, the asymptotic reflection coefficient (29) is zero. This solution is defined as the leading-order term in the asymptotic analysis. When the leading-order term vanishes, the analysis needs to be carried out to the next nonzero term. The next-order term is smaller than the leading order term in most of the spatial domain by the ratio of the local curvature to the acoustic wavenumber, namely, κ/k_0. Thus, the higher order analysis is usually not necessary. It is not pursued here either. Instead, an empirical correction is used in the transition region, which will be discussed in a later section on smooth geometry diffraction. The empirical correction does not precisely recover the analytical solution, leading to the errors shown in the figure, but is much more efficient than the higher order asymptotic analysis.

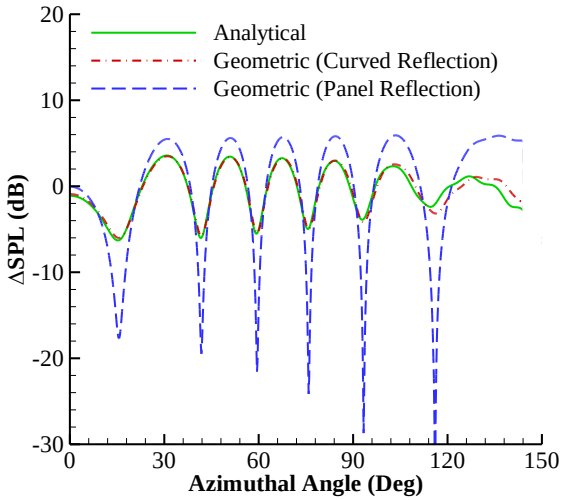

Fig. 3 Sound scattering by a rigid cylinder at 1000 Hz and M=0.4.

The case of panel reflection is included in the comparison by the dashed blue curve to emphasize the importance of the reflection coefficient that accounts for the curved surface geometry. Since geometric acoustics discretizes surface geometry into panels, it is tempting to assume that the reflection can be treated by panel reflection and that the accuracy can be improved by refining the panel elements. This is not the case, as shown by the example in the figure with significant errors between the analytical solutions and the panel reflection results. The panel reflection correctly gives the reflection direction by the Fermat's principle but cannot accurately account for the amplitude changes of the reflected waves, which result from the changes of the cross-section of the ray tubes after reflection. For rigid surfaces, the reflected waves by panels always have the same amplitudes as the incident waves, which is the cause of 6 dB peaks and sharp dips of the blue curve in the figure, a manifestation of perfect constructive and destructive interferences of two waves of equal amplitudes.

IV. Smooth Geometry Diffraction

In geometric acoustics, diffracted rays from a smooth surface are produced by incident rays, which are tangential to the surface of the body. Each tangent ray splits at the point of tangency. One part continues along the path of the incident ray, while the other part travels along the surface of the body as surface waves. These surface waves propagate along the shortest path on the body surface, namely, the geodesic path. At each point on the geodesic path, the surface waves continuously split into two parts, one propagating along the surface and the other leaving the surface along the tangential direction. Thus, a single grazing incident ray gives rise to infinitely many diffracted rays, one of which is shed at each point of the surface ray path. The propagation paths of the diffracted rays, from the source to the surface, and then to the receiver, can be characterized by an extended form of Fermat's principle. The diffracted rays connecting two points on the exterior of the scattering body are the curves joining the two points, which have minimum length

among all curves connecting the two points with an arc on the body surface. From this principle it follows that a diffracted ray consists of three segments, one being a straight line from the source to the tangential point on the surface where the surface wave is launched, the second being a surface arc segment on the geodesics, and the third being a straight line from the ending point of the geodesic segment in its tangential direction to the receiver.

For smooth surfaces such as the wing leading edges and the fuselage in aircraft noise applications, the geometry can be described by a cross section profile and the length of the surface. The cross section can be open, representing a portion of the complete geometry. For the wing, for example, the cross section can be an open curve describing the leading-edge portion of the wing geometry. The length is then in the span direction, along which the cross section is assumed to be approximately invariant. This is not a fundamental restriction on the formulation, because in cases where there are significant variations in the local cross section geometry along the span direction, the geometry can always be divided into multiple segments, each of which has approximately invariant cross section. The diffraction is then the total contributions from all the segments. The use of an open curve to describe the smooth surface diffraction is convenient because it only involves a local region of the total aircraft geometry that is relevant to the diffraction. It also allows discontinuities in the geometry, which are common in aircraft with multiple elements. The surface waves that are responsible for the diffraction, commonly also known as creeping waves, may propagate to the entire geometry and may go around the geometry multiple times. They are, however, heavily dissipated in the propagation due to the radiation off the surface, which increases exponentially with the propagation distance. Thus, the geometry away from the locations where the surface waves are launched is practically irrelevant. The diffraction of acoustic rays by smooth surfaces is illustrated in Fig. 4.

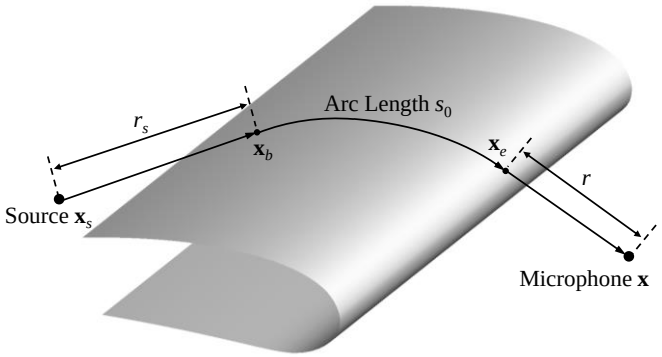

Fig. 4 Illustration of smooth surface diffraction.

The first segment of the ray path is the straight line from the source $\mathbf{x}_s$ to the point $\mathbf{x}_b$, where the surface ray is launched. The propagation of the incident pressure from the source to this point follows the formulations in geometric acoustics and can be denoted by $p_I(\mathbf{x}_b)$. The diffracted pressure can be found by various methods, all under the high frequency approximation, including the geometric diffraction method [9] and the local approximation method [4]. The solution can be expressed as

$$p_D(\mathbf{x}) = p_I(\mathbf{x}_b)\sqrt{\frac{r_s a}{(r+r_s+s_0)r}}e^{\mathrm{i}[\psi(\mathbf{x})-\psi(\mathbf{x}_b)]}\sum_{n=1}^{N} D(\mathbf{x}_e)D(\mathbf{x}_b)e^{-\eta(s_0)} \tag{36}$$

where $p_D(\mathbf{x})$ denotes the diffracted pressure at the field point $\mathbf{x}$, the beginning and the ending point of the surface wave are respectively denoted by $\mathbf{x}_b$ and $\mathbf{x}_e$ with the total arc length between the two being s_0, and r_s and r are the propagation distances, from the source to the surface and from the surface to the microphone, respectively. The summation in the diffracted pressure is over the surface modes, each of which has a different diffraction coefficient and amplitude decay rate. The diffraction coefficient at a point on the geodesic curve is defined by

$$D(s) = e^{\mathrm{i}\pi/24}\left(\frac{1}{2\pi k_0 a(s)}\right)^{1/4}\left(\frac{k_0 a(s)}{2}\right)^{1/6}\frac{1}{\sqrt{-q_n}\,Ai(q_n)} \tag{37}$$

where s is the arc length coordinate along the geodesic path, $a(s)$ is the radius of curvature of the geodesic curve, and q_n is the nth zero of the derivatives of the standard Airy function $Ai(q)$. The loss factor η is defined by

$$\eta = -q_n e^{-\mathrm{i}\pi/6}\left(\frac{k_0}{2}\right)^{1/3}\int_0^{s_0} a^{-2/3}(s)ds\,. \tag{38}$$

The amplitude of the diffraction coefficient defined by (37) is plotted in Fig. 5 as a function of the nondimensional parameter $k_0 a$ for the first four surface modes. The figure shows the reduction of acoustic wave amplitude at the

diffraction point, either at the launching or the radiation point on the surface. The reduction becomes more with increasing frequency, and with increasing modal order. The higher order modes are significantly attenuated by the diffraction process. Thus, for most practical applications, the first mode is sufficient.

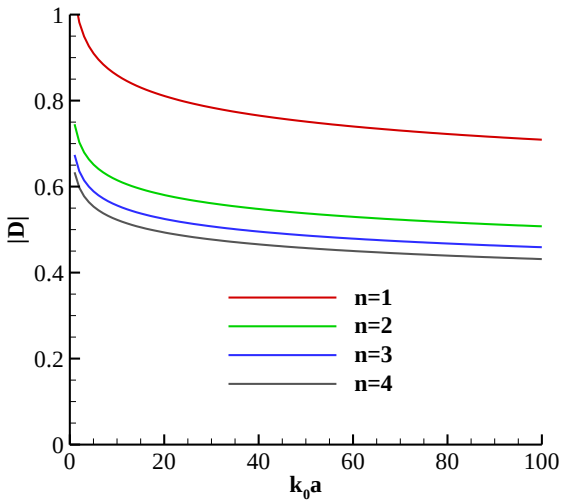

Fig. 5 Smooth geometry diffraction coefficient.

In addition to the attenuation of the acoustic waves at the diffraction points, the acoustic energy is also reduced along the geodesic path on the surface, because the surface wave continuously radiates sound waves back into the acoustic medium along the path, which is accounted for by the exponential factor in (36), resulting in the decay of the surface waves. The decay of the surface waves is given by the loss factor (38). The first four surface modes of the loss factor scaled by the ratio of the radius of curvature to the total arc length are shown in Fig. 6 as a function of the non-dimensional frequency parameter. As is clear from the definition (38), the loss factor involves the integration along the geodesic path, which is geometry dependent. The decay rate increases with frequency and the order of the surface wave modes. The attenuation of the acoustic waves due to the decay of the surface waves depends on the length of the geodesic path traveled by the surface waves.

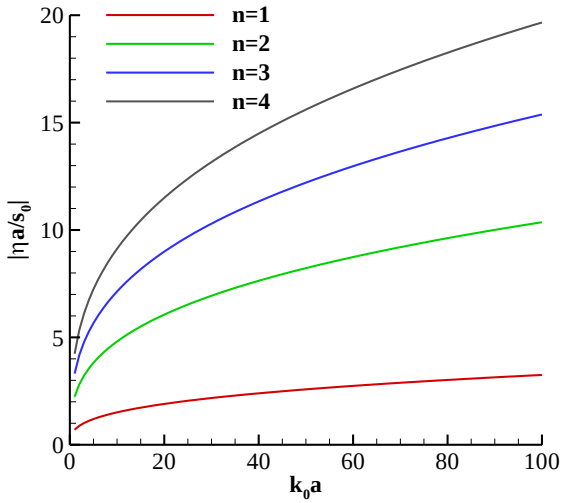

Fig. 6 Magnitude of loss factor of surface waves.

In the solutions (36) to (38), the geometric parameters, including the radius of curvature, the arc length, and the locations of the launching and radiation point of the surface wave, will be determined by the geometry of the diffraction body. The diffraction coefficient (37) and the loss factor (38) are from [9], derived from circular cylinder diffraction and extrapolated for applications of noncircular cylinders. This extrapolation is consistent with geometric acoustics that assumes the wavelengths are shorter than the local radii of the geometry. Thus, the local geometry of an elongated body can be approximated as a portion of a circular cylinder. The variations of the curvature, however, can affect the surface waves, in both the amplitude of the diffraction coefficient and the loss factor, and thus, need to be accounted

for. The curvature effects are related to the properties of the geodesic path followed by the surface waves. For general shapes, this is by no means a trivial task. For aircraft applications where the most important surface elements are characterized by segments with approximately invariant cross sections, the geodesic path and its properties can be derived. The physical conditions to determine the geometric parameters associated with the geodesic curve are the matching of the ray direction with the tangent of the geodesic curve at the launching point and the radiation point of the surface ray, respectively denoted by $\mathbf{x}_b$ and $\mathbf{x}_e$, as illustrated in Fig. 4. The geometry of the diffraction surface is described by the surface contour in the cross-section plane that is perpendicular to the length direction. The cross section can be described by the parametric equation $\mathbf{x} = \mathbf{x}_c(t)$, where t is a length parameter measuring the arc in the cross-section plane, which is indicated by the subscript c. For a given geometry, this parametric equation is given, either by analytical formulas or by data points. On the surface of the diffraction body, the geodesic curve is measured by the arc length on the surface of the three-dimensional body, denoted by s. Thus, a point on the geodesic curve is given by

$$\mathbf{x}_g(s) = \mathbf{x}_c(\alpha s + \gamma) + (\lambda s + \varsigma)\mathbf{e}_2 \,. \tag{39}$$

In this result, the coordinates of the geodesic curve are denoted by $\mathbf{x}_g$ with the subscript g indicating geodesic and $\mathbf{e}_2$ is a unit vector in the length direction. The relation between the arc length of the two-dimensional cross section contour and that of the geodesic curve is given by $t = \alpha s + \gamma$. This relation is also illustrated in Fig. 7, where the cross-section contour $\mathbf{x}_c$ is shown as a function of the two-dimensional contour length t, while the geodesic arc $\mathbf{x}_g$ is shown as a function of the three-dimensional arc length s. The corresponding points on the two curves are also indicated in the figure. The local coordinate system is also shown in the figure that is defined to have $\mathbf{e}_2$ in the direction of the length of the surface. Clearly, the other two components of the coordinates, $\mathbf{e}_1$ and $\mathbf{e}_3$, are in the cross-section plane.

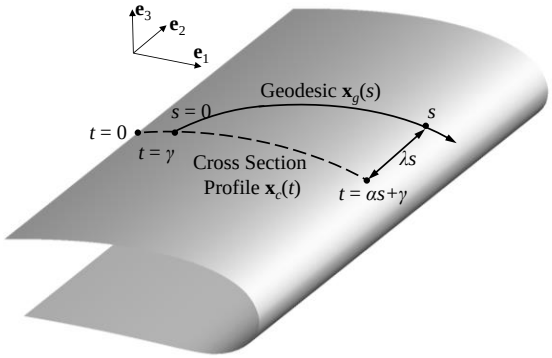

Fig. 7 Relation between cross section contour and geodesic arc.

The set of parameters in the above relations, namely, α, γ, λ and ζ, determines the helical geodesic path. The tangent vector of the geodesic curve is given by the derivative of (39) with respect to the arc length s, namely,

$$\mathbf{t}(s) = \frac{d\mathbf{x}_g(s)}{ds} = \alpha \dot{\mathbf{x}}_c(\alpha s + \gamma) + \lambda \mathbf{e}_2 \tag{40}$$

where the overhead dot on $\mathbf{x}_c$ denotes differentiation with respect to its argument. This vector is also the unit tangent vector because both t and s are arc lengths, in the cross-section plane for the surface contour and on the geodesic curve on the surface of the body, respectively. This leads to $\alpha^2 + \lambda^2 = 1$. At the point $\mathbf{x}_b$, where the surface ray is launched with $s = 0$, the condition of matching the incident ray direction with the tangent of the geodesic curve at this point assumes the form

$$\frac{\mathbf{x}_c(\gamma) + \varsigma \mathbf{e}_2 - \mathbf{x}_s}{r_s} = \alpha \dot{\mathbf{x}}_c(\gamma) + \lambda \mathbf{e}_2 \,. \tag{41}$$

The three components of this vector equation can be found by taking scalar products with the three local unit vectors. There are four unknowns in this vector equation, namely, α, γ, λ and ζ. The additional equation required to solve for the unknowns is provided by the matching of the geodesic curve tangent to the off-surface ray direction at the point $\mathbf{x}_e$ in the form of

$$\frac{\mathbf{x} - \mathbf{x}_c(\alpha s_0 + \gamma) - (\lambda s_0 + \varsigma)\mathbf{e}_2}{r} = \alpha \dot{\mathbf{x}}_c(\alpha s_0 + \gamma) + \lambda \mathbf{e}_2 \,. \tag{42}$$

These two vector equations are coupled together and transcendental, which makes the numerical solutions of the unknowns difficult if the unknowns are solved for simultaneously, especially so in practical applications where the cross-section profile $\mathbf{x}_c$ is given by discrete data points. Thus, a process of deriving the solution and/or decoupling the

equations by analytical methods is highly desirable. This can start with the ratio of the two component equations of (41) in the cross-section plane, immediately leading to

$$\frac{\left(\mathbf{x}_c(\gamma)-\mathbf{x}_s\right)\cdot\mathbf{e}_1}{\left(\mathbf{x}_c(\gamma)-\mathbf{x}_s\right)\cdot\mathbf{e}_3}=\frac{\dot{\mathbf{x}}_c(\gamma)\cdot\mathbf{e}_1}{\dot{\mathbf{x}}_c(\gamma)\cdot\mathbf{e}_3}. \tag{43}$$

This is an equation containing only the single unknown γ, and thus, can be readily solved, either analytically or numerically. For convenience, the solution to this equation is denoted by $\gamma = t_s$. Similarly, the ratio of the two component equations of (42) in the cross-section plane leads to

$$\frac{\left(\mathbf{x}-\mathbf{x}_c(\alpha s_0+\gamma)\right)\cdot\mathbf{e}_1}{\left(\mathbf{x}-\mathbf{x}_c(\alpha s_0+\gamma)\right)\cdot\mathbf{e}_3}=\frac{\dot{\mathbf{x}}_c(\alpha s_0+\gamma)\cdot\mathbf{e}_1}{\dot{\mathbf{x}}_c(\alpha s_0+\gamma)\cdot\mathbf{e}_3} \tag{44}$$

which can be solved to derive the solution for $\alpha s_0+\gamma = t_m$. The quantities t_s and t_m are now known quantities. They are arc lengths of the cross-section contour at two points on the contour, the former at the point where the surface ray is launched by the incidence and the latter at the point where the surface ray radiates to the microphone. By substituting t_s and t_m into the definitions of various quantities discussed above, all quantities of the geodesic path can be derived in closed form formulas.

The asymptotic formulations given above have been extensively validated with the results reported in [25]. An example is given in Fig. 8 for the canonical problem of sound scattering by a cylinder illustrated in Fig. 2 in the previous section. The shielding effect ΔSPL is plotted in Fig. 8 as a function of the azimuthal angle for the shadow region. The diffraction zone is on the opposite side of the source and is defined by the relative locations of the source, the cylinder, and the microphone positions. For the setup shown in Fig. 2, the diffraction zone starts at 144.26 degrees in azimuthal angle. The overall agreement between the asymptotic result and the analytical solution is good, but there is a slight difference in the peak amplitudes of less than 1 dB and a slight shift of the peak azimuthal angles of about 2 degrees. These are due to the approximate treatment of the mean flow effects in the diffraction formulations, which uses the Taylor transformation [26]. The approximation is accurate for low Mach number flows, suitable for aircraft noise applications, and may show errors at moderate Mach numbers, such as the case shown in Fig. 8 where the Mach number is 0.4. That is probably on the upper end of the range for aircraft noise. Even at this moderate Mach number, the errors are small and acceptable for practical applications. In this example, the error in peak amplitudes is less than 2 dB and the error in peak noise angles is less than 3 degrees.

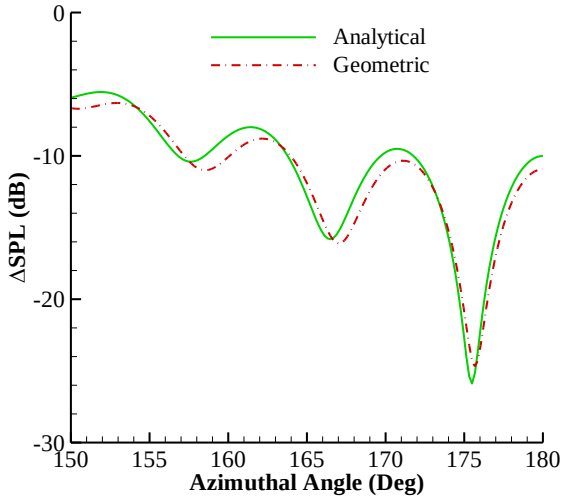

Fig. 8 Diffraction of sound by circular cylinder at M=0.4 and 1000 Hz.

The formulations for the properties of the geodesic path are for an elongated geometry with approximately invariant cross section. For long geometry with noticeable variations in the cross section, such as the leading edge of a wing, the total length can be divided into segments, each of which can be approximated by a constant cross section and has its own geodesic path. The starting and the ending point of a segment, $\mathbf{x}_b$ and $\mathbf{x}_e$, respectively, may not be located within the finite length of the segment. In this case, the surface creeping waves either cannot be generated on or cannot radiate from this segment so that the diffraction contribution from this segment is zero.

The canonical problem of sound scattering by a cylinder is discussed here also to illustrate the need for second-order corrections in the transition region from the insonified to the shadow region. The formulations given in this section for the smooth geometry diffraction in the shadow region have included higher order effects, as illustrated in

Fig. 5 and Fig. 6 by the high-order modes. The reflection coefficient derived in a previous section, however, only includes the first-order terms in the asymptotic analysis, which is given by the result (29). In the transition region where the incidence angle is close to 90 degrees, the reflection coefficient approaches zero, to this order of accuracy, when the incidence angle approaches the grazing angle that is the boundary between the insonified and the shadow region in the definition of geometric acoustics. Thus, the scattered pressure in the transition region is dominantly given by the incident pressure to this first-order accuracy, which corresponds to ΔSPL close to zero. This usually leads to a discontinuity in the results, from ΔSPL=0 on one side of the grazing angle to a finite number on the other side of the grazing angle in the shadow zone, determined by the diffracted pressure. This discontinuity is entirely due to the first-order formulation of the geometric acoustics and can be rectified by various ways. For example, the asymptotic analysis can be extended to the next order. The mathematics of this extension is very involved. Because the second-order effects are small and are confined to the small transition region, it is acceptable to use empirical corrections for practical applications. This is the approach followed here. The approach starts with defining a virtual observation point on the grazing angle boundary, for a given physical observation point in the transition region, with the distance from the virtual point to the source given by the sum of the incident path length and the reflected path length in physical propagation. The diffraction pressure is then computed for this virtual point and the result is used to construct a rapid falloff correction, as a function of the incidence angle. As the incident angle approaches the grazing angle, the corrected result approaches the diffraction result on the grazing angle and the correction rapidly decreases to zero for angles away from the grazing angle. The geometry in the transition region for the second-order correction is illustrated in Fig. 9, showing the definitions of various spatial coordinates.

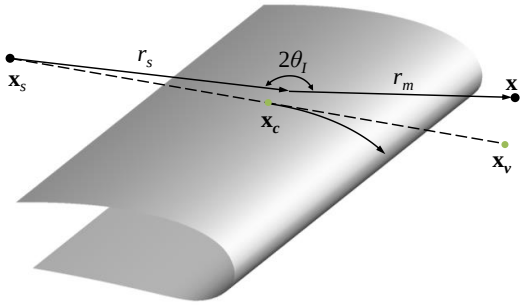

Fig. 9 Illustration of transition region geometry.

For an observation point in the transition region, denoted by the coordinate vector $\mathbf{x}$, the sound from the source located at $\mathbf{x}_s$ will be reflected by the surface at the point where the angle between the incident and the reflected propagation is $2\theta_I$. For this observation point, a virtual point can be defined, denoted by $\mathbf{x}_v$, according to

$$\mathbf{x}_v = \mathbf{x}_s + (r_s + r_m)\frac{\mathbf{x}_c - \mathbf{x}_s}{|\mathbf{x}_c - \mathbf{x}_s|} \tag{45}$$

where r_s and r_m are the distances from reflection point to the source and the microphone, respectively, for the physical propagation, and $\mathbf{x}_c$ is the point at which the line from $\mathbf{x}_s$ to $\mathbf{x}_v$ touches the surface. For the virtual point $\mathbf{x}_v$, which is located on the grazing angle, the diffracted pressure can be calculated according to the formulations given earlier in this section. The total pressure at the physical observation point can be constructed as

$$p(\mathbf{x}) = p_I(\mathbf{x}) + p_R(\mathbf{x}) + \frac{p_I(\mathbf{x})}{p_I(\mathbf{x}_v)} e^{-\mu\cos\theta_I}\left(p_D(\mathbf{x}_v) - p_I(\mathbf{x}_v)\right) \tag{46}$$

where the incident, the reflected, and the diffracted pressure are denoted by the subscript *I*, *R*, and *D*, respectively, and the locations of the pressures are indicated by their arguments. The falloff from the grazing angle is controlled by the incidence angle θ_I and the factor μ, which can be given a large value to ensure the effects are confined to the transition region. It is also desirable to make this factor a function of frequency so that the accuracy of the correction is uniform in frequency.

To illustrate the effects of the correction, an example is given in Fig. 10 for the canonical problem shown in Fig. 2 for which some results are discussed in Fig. 3 and Fig. 8. In this figure, the scattered pressure, normalized by the incident pressure, is plotted in the azimuthal angle domain that includes the transition region in the vicinity of the grazing angle of 144.26 degrees. The dashed blue curve represents the results from the geometric acoustics formulation to the first order in the transition region. The discontinuity is about 5 dB at the grazing angle. The dash-dot red curve shows the results of the asymptotic formulation with second-order corrections in the transition region, which eliminates the discontinuity. The second order corrections do not have any impact in regions away from the transition region, as expected since the leading order term in the reflection coefficient is nonzero in these regions.

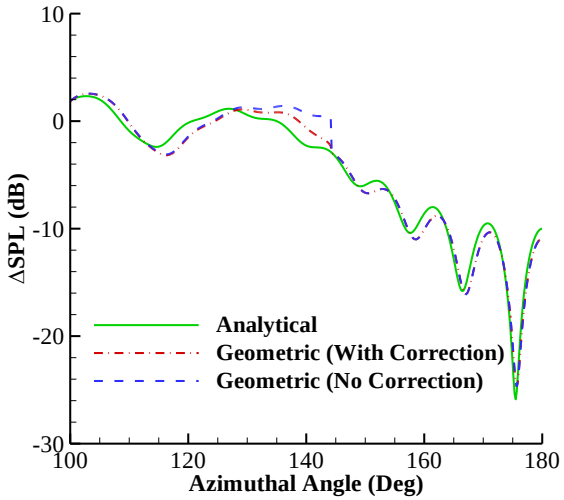

Fig. 10 Effect of second-order corrections in transition region.

V. Sharp Edge Diffraction

Sharp edge diffraction is a prominent feature in aircraft noise scattering because of the sharp trailing edges of the wings and high-lift system elements. For such geometry, the edges are usually straight and are many wavelengths long. Thus, the diffraction theory for an infinitely long wedge is applicable, consistent with the high frequency approximation. The diffraction occurs when the propagation of sound waves from a source is interrupted by a sharp wedge. In terms of ray acoustics, a ray that hits a wedge can no longer carry all its acoustic energy along the original ray path. Instead, the acoustic energy is redistributed among many rays emanating from the diffraction point where the incidence ray hits the wedge line, as if the diffraction point is a highly directional point source. The rays from the diffraction point form a conic surface, which has its apex at the diffraction point, its axis coinciding with the wedge line, and its angle equal to the angle between the incidence ray and the wedge line. The diffraction features are illustrated in Fig. 11, where the incidence ray is diffracted into many rays by the wedge.

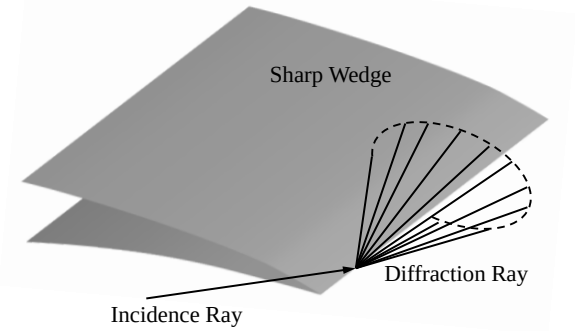

Fig. 11 Illustration of sharp wedge diffraction.

There are various mathematical ways to derive the formulations for sharp wedge diffraction in the high frequency limit and the formulas may assume various forms, which are all equivalent to the leading order. One such method is by using image sources and complex angle integration [4], which is based on earlier research [8], [23]. For a wedge with a straight edge line, the edge line can be specified by two points. Since the practical applications always involve finite length edges, it is convenient to specify the edge line by the beginning and the ending point of the wedge segment, denoted by $\mathbf{x}_b$ and $\mathbf{x}_e$, respectively, and $\hat{\mathbf{s}}$ denotes the unit tangent of the edge line. A point on the edge line can then be specified as $\mathbf{x}_w(s) = s\hat{\mathbf{s}} + \mathbf{x}_b$. Here, $\mathbf{x}_w$ denotes the coordinates of the wedge line as a function of the segment length s which is set to zero at the beginning point $\mathbf{x}_b$ and increases towards the ending point $\mathbf{x}_e$. The geometry of the edge diffraction is illustrated in Fig. 12. In the figure, the source location is denoted by $\mathbf{x}_s$ and the microphone location by $\mathbf{x}$. The coordinate of the diffraction point is represented by $\mathbf{x}_w(s^*)$, which can be found by using the diffraction condition that the incidence angle and the diffraction angle, both with respect to the edge line, must be equal, as indicated in the figure by the angle θ_I.

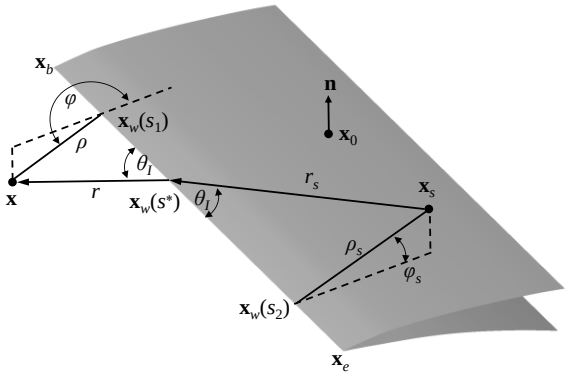

Fig. 12 Geometry of sharp wedge diffraction.

To find the diffraction point $\mathbf{x}_w(s^*)$, it is convenient to first derive the normal distance from the source to the edge line, namely, between the source $\mathbf{x}_s$ and the point $\mathbf{x}_w(s_2)$, which can be found explicitly as

$$\rho_s = \left| \left[\left(\mathbf{x}_s - \mathbf{x}_b \right) \cdot \hat{\mathbf{s}} \right] \hat{\mathbf{s}} + \mathbf{x}_b - \mathbf{x}_s \right| . \tag{47}$$

The same process can also be applied to the microphone location $\mathbf{x}$, leading to the normal distance between the microphone and the edge line in the form of

$$\rho = \left| \left[\left(\mathbf{x} - \mathbf{x}_b \right) \cdot \hat{\mathbf{s}} \right] \hat{\mathbf{s}} + \mathbf{x}_b - \mathbf{x} \right| . \tag{48}$$

The two distance quantities are both shown in Fig. 12.

At the diffraction point $\mathbf{x}_w(s^*)$, the edge line length is denoted by s^*, which must satisfy the equal angle diffraction condition. Thus, it follows that

$$\frac{\rho}{s^* - s_1} = \frac{\rho_s}{s_2 - s^*} . \tag{49}$$

This can be solved immediately to yield

$$s^* = \frac{s_1 \rho_s + s_2 \rho}{\rho + \rho_s} . \tag{50}$$

From the results derived above, the diffraction point is determined by the relative positions of the source and the microphone, in relation to the wedge line.

The diffraction pressure can be written in the form consistent with the ray tracing methodology in which the incidence ray propagates from the source to the diffraction point and gets diffracted into rays emanating from the diffraction point. Thus, it follows that

$$p_D(\mathbf{x}) = p_I(\mathbf{x}_w^*) \frac{r_s}{r + r_s} e^{\mathrm{i}k_0 r} D(\mathbf{x}, \mathbf{x}_s) . \tag{51}$$

This is the diffraction pressure p_D at the microphone location $\mathbf{x}$ expressed in terms of the incidence pressure p_I at the diffraction point, denoted by

$$\mathbf{x}_w^* = \mathbf{x}_w(s^*) \tag{52}$$

with s^* given by (50).

The diffraction coefficient D in the result (51) is given by

$$D(\mathbf{x}, \mathbf{x}_s) = \frac{\sin \nu\pi}{\sqrt{2}} e^{\mathrm{i}\pi/4} \sum_{+,-} \frac{A_D\left[\chi(\varphi \pm \varphi_s)\right]}{\sqrt{1 - \cos(\nu\pi)\cos\nu(\varphi \pm \varphi_s)}} . \tag{53}$$

Here, the parameter ν is the wedge index that specifies the wedge angle with the relation $\nu = \pi/(2\pi - w)$, where w is the wedge angle. The dependence of the diffraction coefficient on the microphone and the source location is represented in the two angular parameters φ and φ_s, which are both illustrated in Fig. 12. The diffraction coefficient (53) involves the function denoted by A_D, which is the diffraction integral defined by

$$A_D(\chi) = \frac{1}{\pi} \int_{-\infty}^{\infty} \frac{e^{-u^2}}{\sqrt{\pi}\chi - (1 - \mathrm{i})u} du . \tag{54}$$

When this is applied to the diffraction coefficient, the argument χ is defined by

$$\chi(\varphi \pm \varphi_s) = \frac{1}{\nu}\sqrt{\frac{k_0 \rho_s \rho}{\pi(r_s + r)}}\,\frac{\cos(\nu\pi) - \cos\nu(\varphi \pm \varphi_s)}{\sqrt{1 - \cos(\nu\pi)\cos\nu(\varphi \pm \varphi_s)}}\,. \tag{55}$$

The two signs correspond to the two terms in the summation in (53).

The diffraction integral defined by (54) is an important and well-known feature in sharp edge scattering. An inevitable feature of the scattering involving a sharp edge is the division of the spatial domain into various zones, such as the insonified zone, the reflection zone, and the shadow zone. The zones are determined by how the various components of the scattering propagate and are intuitively easy to understand. The divisions between the zones are, however, not defined with clear boundaries. In fact, the transition from one zone to another is gradual and continuous. This smooth transition is accomplished by the diffraction integral, which is plotted in Fig. 13, showing both its real and imaginary part as a function of the parameter χ. The transition is at locations near $\chi = 0$, where the smooth curves connect the two regions. From the definition (55), the zeros of the parameter χ are given by the vanishing of the numerator in the definition, which is equivalent to

$$\varphi \pm \varphi_s = \pi\,. \tag{56}$$

Thus, there are two transitions in the azimuthal angle domain, one being the grazing incidence when the incident and the diffracted waves are in the same direction and the other being the angle between the reflection zone and the direct radiation zone.

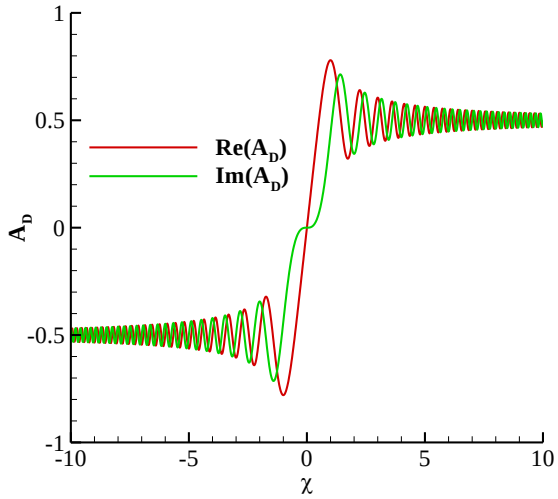

Fig. 13 Diffraction integral for sharp wedge scattering.

The formulations given above have been validated in [25] with various cases. To illustrate, the simple case of diffraction by a semi-infinite plate is shown in Fig. 14, where a point source is located 1 meter above the plate and 1 meter away from the edge and the microphones are placed below the plate on an arc with a radius of 10 meters from the edge of the semi-infinite plate. The microphones are specified by the azimuthal angle, defined to be zero in the direction of the plate extension and to be -180 degrees on the plate on the opposite side of the source. In this setup, the shadow region determined by the line of sight is from -45 to -180 degrees in the azimuthal angle.

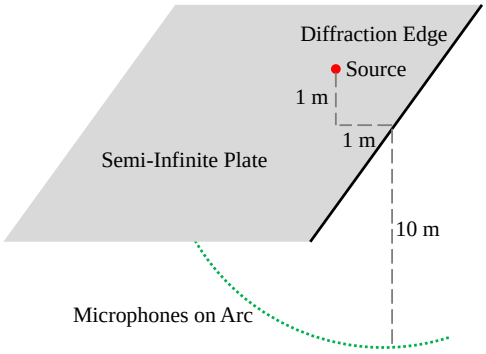

Fig. 14 Setup of diffraction by semi-infinite plate.

The results for the semi-infinite plate are shown in Fig. 15, where the shielding effect ΔSPL is plotted as a function of the azimuthal angle at 1000 Hz. The analytical solutions are derived by wavenumber integration and the method of Wiener-Hopf factorization [6]. The comparisons between the analytical solution and the asymptotic result are given by the solid green and the dash-dotted red curve, showing very good agreement. The result from the method of Kirchhoff integration is also shown in Fig. 15 by the dashed blue curve. It is included to reveal the inadequacy of this method that has attracted some attention in recent years [14], [15] but has not been able to achieve satisfactory accuracy. This is due to the fundamental assumptions of the method that ignore the contributions from the scattering surfaces in the shadow of the source and approximate the pressure on the insonified surfaces by the incident pressure. This may be a reasonable approximation for measurement locations with direct and/or reflected sound from the source, where the contributions from the shadow surface elements are of secondary order. For measurement locations in the shadow region, however, there is no direct and reflected sound from the source and the contributions from the shadow surface elements are of leading order. By neglecting these leading order contributions, the Kirchhoff method inevitably underpredicts the noise levels in the shadow region, illustrated by the large discrepancies between this method and the analytical solution in Fig. 15 in the shadow region between -45 and -180 degrees.

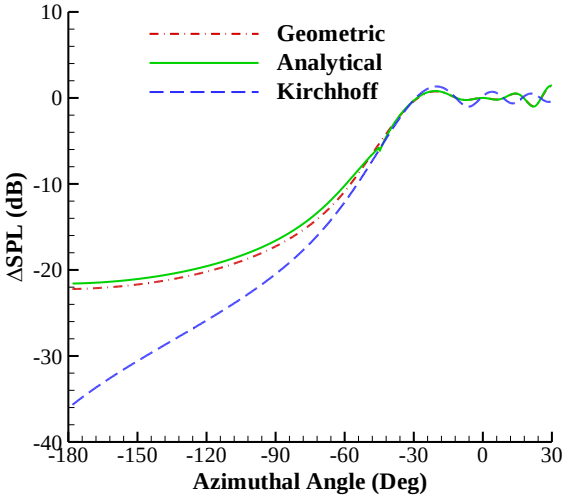

Fig. 15 Sharp edge diffraction by semi-infinite plate at 1000 Hz.

For a wedge of finite length, the diffraction point must be on the edge line between the starting and the ending point of the wedge for the diffraction to occur. Thus, the condition is

$$0 \le s^* \le \left|\mathbf{x}_e - \mathbf{x}_b\right| . \tag{57}$$

For an infinitely long wedge, this condition is of course automatically satisfied but for finite length wedges in practical application, the condition needs to be checked. If not satisfied, the diffraction point is not on the finite wedge line. In this case, the diffraction is not given by the formulas derived above. Instead, it is given by the next-order solution in the asymptotic analysis. This second-order solution is needed only if the leading-order term formulated in this section is zero. Otherwise, the second-order contribution is smaller than the leading order by a factor inversely proportional to frequency.

To account for the effects of finite dimensions, a simple model can be used to modify the strength of the apparent diffraction sources. The physical reasoning is that the diffraction strength formulated above in this section can be achieved only if the wedge surface is semi-infinite with pressure fluctuations on the entire surface, which in turn can be attributed to acoustic energy of the incident waves impinging on the entire surface. The diffraction strength is attributed to the aggregate effects of the incident acoustic energy on the surface. For wedges of finite dimensions, the smaller surface area leads to less incident energy impinging on the surface, which in turn leads to reduced diffraction strength. For a source located at **y**, the incident waves can be described by the acoustic velocity potential ϕ

$$\phi(\mathbf{x}) = \frac{1}{4\pi\left|\mathbf{x}-\mathbf{y}\right|} e^{ik_0|\mathbf{x}-\mathbf{y}|} \tag{58}$$

where **x** is the coordinate on the surface. From this, the energy flux can be written as

$$\frac{\partial\phi}{\partial n} p^* = \frac{c_0\rho_0 k_0^2}{(4\pi)^2} \frac{1}{\left|\mathbf{x}-\mathbf{y}\right|^2} \frac{\partial\left|\mathbf{x}-\mathbf{y}\right|}{\partial n} \tag{59}$$

which is the product of the normal velocity and the acoustic pressure. The surface normal direction is indicated by n. The total incident energy is then the integration over the surface, namely,

$$E = \int_S \frac{1}{|\mathbf{x}-\mathbf{y}|^2} \frac{\partial |\mathbf{x}-\mathbf{y}|}{\partial n} dS \tag{60}$$

where E denotes the total incident energy, S is the surface area, and the proportional constants in the energy flux (59) have been omitted since the results will be cast in nondimensional forms with respect to the semi-infinite surface with the constants all cancelled in the normalization. For a semi-infinite surface, the integration simply leads to

$$E_0 = \pi + 2 \arctan \frac{y_1}{y_3} \tag{61}$$

where E_0 is the incident energy for a semi-infinite surface, and y_1 and y_3 are the source coordinates in the direction normal to the wedge line and the direction normal to the surface. The integration can be carried out for a finite surface, with the result

$$E = \sum_{n=1}^{4} \arctan \frac{C_n B_n}{y_3 \sqrt{C_n^2 + B_n^2 + y_3^2}} \tag{62}$$

where the coefficients C_n and B_n are introduced to simplify the mathematical expression. They are given in Table 1, in which C_0 and B_0 are respectively the chord and the span of the surface and y_2 is the source coordinate in the span direction. From these results, the correction for wedges of finite dimensions is defined as E/E_0.

Table 1 Coefficients for finite wedge effects.

n	C_n	B_n
1	C_0 - y_1	$0.5B_0$ - y_2
2	y_1	$0.5B_0$ - y_2
3	C_0 - y_1	$0.5B_0$ + y_2
4	y_1	$0.5B_0$ + y_2

VI. Source Coherence

Since geometric acoustics follows individual rays, or propagation paths, source coherence can be naturally accounted for because the differences in ray path lengths represent different source times of the ray contributions. The source coherence effects can then be calculated by the differences in ray path lengths when the ray contributions are summed at the measurement locations. To illustrate this concept, a simple case is shown in Fig. 16, where the sound from a source reaches the microphone through two paths, one direct radiation and the other reflection by a surface element. The source is defined by its strength $q(t)$ as a function of time t and its coherence feature is represented by the source autocorrelation, which, for statistically stationary sources, assumes the form of

$$Q(\tau) = \langle q(t) q(t+\tau) \rangle \tag{63}$$

where Q is the autocorrelation, τ is the time delay, and the angle brackets indicate ensemble average. The general properties of the autocorrelation are the maximum achieved at time delay equal to zero and the falloff from the maximum as the time delay increases. The rate of the falloff characterizes the degree of the source coherence, with more rapid falloff for more incoherent sources.

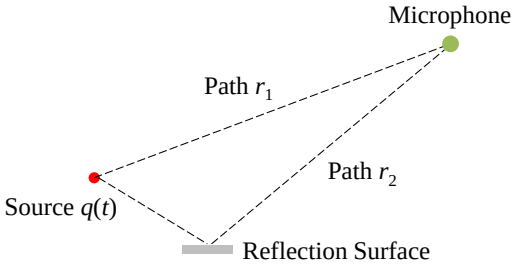

Fig. 16 Illustration of sound propagation paths.

In geometric acoustics, the sound pressure at the microphone location consists of two contributions, corresponding to the two propagation paths illustrated in the figure, with each contribution given by the source strength q at a retarded time, modified by the spherical spreading. Thus,

$$p(t) = \frac{1}{r_1} q(t - r_1 / c_0) + \frac{1}{r_2} q(t - r_2 / c_0) \tag{64}$$

where r_1 and r_2 are the lengths of the two propagation paths, and for simplicity, the source strength q is assumed to contain various properties such as directivity, amplitude, and phase. The squared pressure with ensemble average is then given by

$$\left\langle p^2(t) \right\rangle = \frac{1}{r_1^2} Q(0) + \frac{1}{r_2^2} Q(0) + \frac{2}{r_1 r_2} Q\left(\frac{r_2 - r_1}{c_0} \right) \tag{65}$$

where the first two terms are the two contributions from the two paths independent of each other, and the last term is the contribution from the interactions of the two, determined by the source correlation function and the length difference of the two propagation paths. From the general properties of the source autocorrelation, the interaction terms achieve maximum amplitude with either very coherent sources or small path length differences. On the other hand, this term is small with either very incoherent sources or large path length differences.

For the implementation of the source coherence in geometric acoustics, the acoustic pressure generated by N sources, each of which has contributions from K propagation paths, has the general form

$$p(\omega) = \sum_{n=1}^{N} \sum_{k=1}^{K(n)} \frac{C_{nk}}{r_{nk}} q_n(\omega) e^{\mathrm{i}\omega r_{nk}/c_0} \tag{66}$$

where the summation index n is over the N sources with the individual source strength represented by $q_n(\omega)$, and the index k is over the $K(n)$ propagation paths for each source. For distributed sources, the source summation in n is replaced by a source integration and the dependence on the index n becomes a dependence on the coordinates of the source distribution. The length of the propagation path, denoted by r_{nk}, is a function of both the source and the propagation path. The acoustic pressure is also affected by the reflections and/or diffractions along the propagation path, if any. These are collectively denoted by the coefficient C_{nk}, which is equal to the product of the reflection coefficients and the diffraction coefficients along a propagation path.

From the general solution for the acoustic pressure, the acoustic spectrum can be constructed by the definition

$$\Pi(\omega) = \left\langle p(\omega) p^*(\omega) \right\rangle \tag{67}$$

where Π denotes the acoustic spectrum and the symbol $*$ indicates complex conjugate. By substituting the general solution (66) into this definition and performing the ensemble average, it follows that

$$\Pi(\omega) = \sum_{n=1}^{N} \sum_{k=1}^{K(n)} \sum_{n'=1}^{N} \sum_{k'=1}^{K(n')} \frac{C_{nk}}{r_{nk}} \frac{C_{n'k'}^*}{r_{n'k'}} Q\left(k_0 (r_{nk} - r_{n'k'}) \right) e^{\mathrm{i}\omega (r_{nk} - r_{n'k'})/c_0} \tag{68}$$

where the source coherence function Q is determined by the differences in the propagation paths, normalized by the acoustic wavelength. From the general properties of the coherence function, the contributions involving different propagation paths are affected by the source coherence, except for perfect coherent and perfect incoherent sources. For the former, the coherence function is constant, and the result reduces to

$$\Pi(\omega) = \left| \sum_{n=1}^{N} \sum_{k=1}^{K(n)} \frac{C_{nk}}{r_{nk}} Q(0) e^{\mathrm{i}\omega r_{nk}/c_0} \right|^2 \tag{69}$$

which is the squared total pressure, containing all the interferences between the propagation paths and sources. For the latter where the sources are perfectly incoherent, the coherence function is zero for nonzero argument so that the result limits to

$$\Pi(\omega) = \sum_{n=1}^{N} \sum_{k=1}^{K(n)} \frac{1}{r_{nk}^2} \left| C_{nk} \right|^2 Q(0) \tag{70}$$

which is simply the summation of the squared pressures from the individual paths without any interference effects.

To demonstrate the effects of source coherence, an example of noise shielding is given for the hybrid wing body (HWB) aircraft model shown in Fig. 17, together with the noise sources located at the engine exit plane that is 2.5 nozzle diameters upstream of the aircraft trailing edge, indicated by the green dots in the figure. This is a configuration included in a NASA wind tunnel test [26] with the model at 5.8% of a full-scale aircraft, in which the noise is generated by impinging jets enclosed in a nacelle, simulating engine broadband noise. Thus, the noise sources are very incoherent. It is also one of the cases included in the validations in [25].

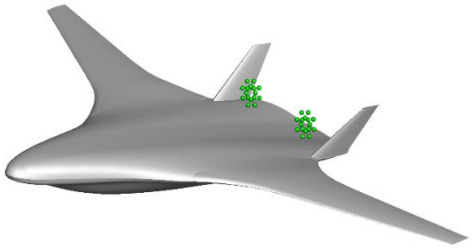

Fig. 17 HWB model geometry and sources.

The effects of noise shielding for this configuration are predicted and shown in Fig. 18, where the shielding ΔSPL is plotted as a function of the polar angle, defined from the upstream direction, in the aircraft centerline plane. Both predictions and test data are shown in the figure at 20 kHz. The predictions are for two source characterizations, one coherent and the other incoherent, respectively represented by the dashed blue and the solid red curve. The incoherent predictions agree well with the test data, as expected since the impinging jets in the test are incoherent noise sources. On the other hand, the coherent predictions show larger errors, up to 10 dB overprediction at angles with strong constructive interference and up to 7 dB underpredictions at angles of strong destructive interferences.

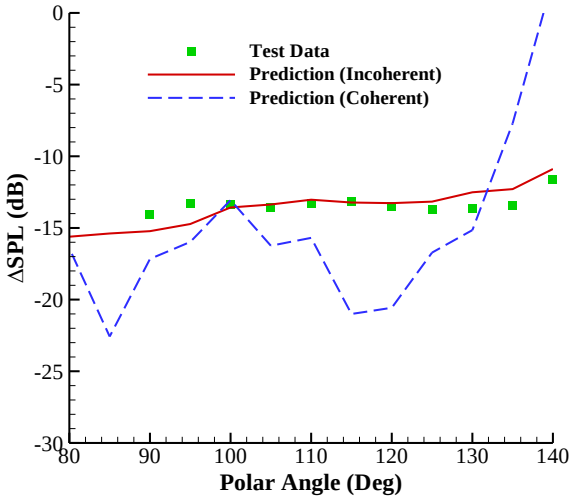

Fig. 18 Noise shielding by HWB aircraft.

VII. Conclusion

In this paper, some features of geometric acoustics have been discussed, to develop a methodology in the framework of geometric acoustics for applications in aircraft noise scattering. A general formula has been derived for the reflection coefficient that accounts for irregular curved surfaces with surface impedance and imbedded in mean flows, which are all important features in aircraft noise. The formulas for diffraction of canonic geometry shapes have been modified/corrected for geometry shapes of finite dimensions. Use has been made of the elongated components in aircraft geometry to develop efficient calculation for the properties of the geodesic paths, needed for the calculation of diffraction by smooth geometry. The coherence features of the sources have been included in the methodology, facilitated by the acoustic ray formulation of geometric acoustics, representing a significant advantage of geometric acoustics in aircraft noise scattering calculations.

Though the validations of the individual features and the overall prediction methodology will be given in a future systematic study, some simple examples have been presented to illustrate the accuracy, and, more importantly, to demonstrate the effects of the discussed features. These have included the importance of curved surface reflection in comparison with analytical solutions and with the approximation of panel reflection. While the agreement between the analytical solutions and the formulation for curved surface reflection is very good, it has been shown that the panel reflection approximation greatly overpredicts the interference between the incident and the reflected waves, leading to large errors. The effects of second-order corrections in the transition region between insonified and shadow zones have been shown to be needed to render the results continuous. The errors in the diffraction by smooth geometry in shadow zones due to the use of the approximate method of the Taylor transformation to account for mean flows have

been discussed. For sharp geometry diffraction, the advantage of the wedge diffraction formulation over the method of Kirchhoff integration has been demonstrated and discussions have been given for the cause of the large errors in the latter method. The importance of source coherence in sound scattering calculations has been demonstrated with comparisons between the coherent and the incoherent calculations, together with comparisons with wind tunnel test data.

Acknowledgments

The support of the NASA Advanced Air Transport Technology Project is gratefully acknowledged. Dr. Florence Hutcheson is thanked for providing the hybrid wing body aircraft model test data.

References

[1] Keller, J. B., "Geometrical Theory of Diffraction," *Journal of the Optical Society of America*, Vol. 52, No. 2, pp 116–130, 1962.
[2] Keller, J., "Rays, Waves and Asymptotics," *Bulletin of the Am. Math. Soc.,* Vol. 84, No. 5, pp 727-750, 1978.
[3] Lewis, R. M., and Boersma, J., "Uniform Asymptotic Theory of Edge Diffraction," *Math. Phys*., Vol. 10, No. 12, pp 2291–2305, 1969.
[4] Pierce, A. D., "Acoustics: An Introduction to its Physical Principles and Application," McGraw-Hill, 1981.
[5] Dowling, A. P., and Ffowcs Williams, J. E., "Sound and Sources of Sound," Ellis Horwood Publishers, 1983.
[6] Crighton, D. G., Dowling, A. P., Ffowcs Williams, J. E., Heckl, M., and Leppington, F. G., "Modern Methods in Analytical Acoustics," Springer-Verlag, 1992.
[7] Morse, P. M., and Ingard, K. U., "Theoretical Acoustics," McGraw-Hill, 1968.
[8] Sommerfeld, A., "Lectures on Theoretical Physics," *Optics*, Vol. IV, Academic Press, 1954.
[9] Levy, B., and Keller, J. B., "Diffraction by a Smooth Object," *Communications on Pure and Applied Mathematics*, Vol. 12, pp. 159–209, 1959.
[10] Agarwal, A., Dowling, A. P., Shin, H. C., Graham, W., and Sefi, S., "A Ray Tracing Approach to Calculate Acoustic Shielding by the Silent Aircraft Airframe," 12th AIAA/CEAS Aeroacoustics Conference (27th AIAA Aeroacoustics Conference), AIAA 2006-2618, May 2006.
[11] Agarwal, A., and Dowling, A. P., "The Calculation of Acoustic Shielding of Engine Noise by the Silent Aircraft Airframe," 11th AIAA/CEAS Aeroacoustics Conference (26th AIAA Aeroacoustics Conference), AIAA 2005-2996, May 2005.
[12] van Rens, J. R. P., van Rens, B. J. E., Holten, T., and Ruijgrok, G. J. J., "Sound Level Prediction Using a Ray Tracing Algorithm for a Blended-Wing-Body," 6th AIAA/CEAS Aeroacoutics Conference. AIAA 2000-2069, June 2000.
[13] Lummer, M., "Maggi-Rubinowicz Diffraction Correction for Ray-Tracing Calculations of Engine Noise Shielding," 14th AIAA/CEAS Aeroacoustics Conference (29th AIAA Aeroacoustics Conference), AIAA 2008-3050, May 2008.
[14] Colas, D. F. M., "A Diffraction Integral Based Turbomachinery Noise Shielding Method," Master's Thesis, Department of Aeronautics and Astronautics, Massachusetts Institute of Technology, 2011.
[15] Guo, Y. P., Pope, D. S., Burley, C. L., and Thomas, R. H., "Aircraft System Noise Shielding Prediction with a Kirchhoff Integral Method," 23rd AIAA/CEAS Aeroacoustics Conference, AIAA 2017-3196, June 2017.
[16] Ganci, S., "A General Scalar Solution for the Half-plane Problem," *J. Mod. Opt*., 42(8):1707–1711, August 1995.
[17] Umul, Y. Z., "Young-Kirchhoff–Rubinowicz Theory of Diffraction in the Light of Sommerfeld's Solution," *J. Opt. Soc. Am.* A, 25(11):2734–2742, November 2008.
[18] Waterhouse, R. V., "Diffraction Effects in a Random Sound Field," *J. Acoust. Soc. Am*., Vol. 35, No. 10, pp 1610-1620, 1963.
[19] MacDonald, H. M., "A Class of Diffraction Problems," *Proc. Lond. Math. Soc*., Vol. 14, pp 410-427, 1915.
[20] Bromwich, A., "Diffraction of Waves by a Wedge," *Proc. Lond. Math. Soc*., Vol. 14, pp 450-463, 1915.
[21] Whipple, F. J. W., "Diffraction by a Wedge and Kindred Problems," *Proc. Lond. Math. Soc*., Vol. 16, pp 94-111, 1917.
[22] Biot, M. A., and Tolstoy, I., "Formulation of Wave Propagation in Infinite Media by Normal Coordinates with an Application to Diffraction," *J. Acoust. Soc. Am.*, Vol. 29, pp 381-391, 1957.
[23] Sommerfeld, A., "Mathematical Theory of Diffraction," *Math. Ann*., Vol. 47, pp 317-374, 1896.
[24] Bleistein, N., and Handelsman, R. A., "Asymptotic Expansion of Integrals," Dover Publications Inc., New York, 1975.
[25] Thomas, R. H. and Guo, Y., "Systematic Validation of the PAAShA Shielding Prediction Method," Accepted for publication in International Journal of Aeroacoustics, 2022.
[26] Taylor, K., "A Transformation of the Acoustic Equation with Implications for Wind Tunnel and Low-Speed Flight Tests," *The Royal Society of London. Series A, Mathematical and Physical Sciences*, Vol. 363, pp 271–281, November 1978.
[27] Hutcheson, F. V., Brooks, T. F., Burley, C. L., Bahr, C. J., Stead, D. J. and Pope, D. S., "Shielding of Turbomachinery Broadband Noise from a Hybrid Wing Body Aircraft Configuration,", 20th AIAA/CEAS Aeroacoustics Conference, AIAA 2014-2624, June 2014.